



Fabrication of platinum-deposited carbon nitride nanotubes by a one-step solvothermal treatment strategy and their efficient visible-light photocatalytic activity



Kexin Li^a, Zhenxing Zeng^a, Liushui Yan^a, Shenglian Luo^{a,*}, Xubiao Luo^a, Mingxin Huo^b, Yihang Guo^b

^a Key Laboratory of Jiangxi Province for Persistent Pollutants Control and Resources Recycle, Nanchang Hangkong University, Nanchang 330063, PR China

^b Jilin Engineering Research Centre for Municipal Wastewater Treatment and Water Quality Protection, School of Environment, Northeast Normal University, Changchun 130117, PR China

ARTICLE INFO

Article history:

Received 2 August 2014

Received in revised form 9 October 2014

Accepted 14 October 2014

Available online 22 October 2014

Keywords:

Noble metal

Graphitic carbon nitride

Nanotubes

Hydrogen evolution

Organic pollutant degradation

ABSTRACT

A series of platinum nanoparticles-deposited carbon nitride nanotubes (Pt/C₃N₄ NTs) was fabricated by a simple one-step solvothermal treatment strategy using graphite carbon nitride (g-C₃N₄) and chloroplatinic acid (H₂PtCl₆·6H₂O) as precursors. The morphology, porosity, phase and chemical structure, and optical and electronic properties of Pt/C₃N₄ NTs were well characterized. Compared with bulk g-C₃N₄, the as-prepared Pt/C₃N₄ NTs exhibited efficient photocatalytic activity toward hydrogen evolution from water-splitting and aqueous *p*-chlorophenol degradation under visible-light irradiation ($\lambda > 420$ nm) as a result of their unique tubular nanostructure and the synergic effect of Pt nanoparticles. Subsequently, the activities of simultaneous hydrogen evolution with organic pollutant degradation were also tested using as-prepared Pt/C₃N₄ NTs under the representative organic pollutants *p*-chlorophenol, *p*-nitrophenol, methylene blue, or rhodamine B as electron donors. Finally, the photocatalytic mechanisms in three different photocatalytic systems were discussed.

© 2014 Elsevier B.V. All rights reserved.

1. Introduction

Energy crisis and environmental pollution are two serious problems that humans face in the process of sustainable development [1–3]. In recent decades, the development of semiconductor photocatalytic materials and photocatalytic technique brought new opportunities and challenges for solving the energy and environmental problems [4–7]. Various photocatalytic systems have been widely studied such as hydrogen evolution, organic pollutant degradation, and carbon dioxide reduction [8–10]. Since its discovery in 2008, the application of the visible-light photocatalytic activity of graphite carbon nitride (g-C₃N₄) as an effective metal-free semiconductor photocatalyst was extensively developed [11–15]. However, visible-light photocatalytic activity of g-C₃N₄ is low due to their bulk structure and low quantum efficiency. As such, many researchers were devoted to develop g-C₃N₄-based materials with high visible-light photocatalytic activity [16,17]. Nanostructure design and noble metal deposition are two

effective strategies to improve the photocatalytic activity of semiconductor photocatalysts. Therefore, some researchers improved the visible-light photocatalytic activity of g-C₃N₄ by nanostructure design [18–20]. Because nanostructural g-C₃N₄ possesses larger number of active sites and exhibits smaller mass transfer resistance in the course of photocatalytic reaction compared with bulk g-C₃N₄. Other researchers tried to deposit noble metals on the surface of g-C₃N₄ for capturing photoexcited electrons, thereby decreasing the photogenerated electron (e[−])–hole (h⁺) pair recombination probability [21–23]. Unfortunately, some problems exist in the above modification methods: first, the procedure for the nanostructure design is complex and toxic solvents are used in the preparation process. Second, noble metal nanoparticles are directly deposited on the surface of bulk g-C₃N₄ by traditionally chemical or optical reduction methods; therefore, the electron capturing effect by noble metal nanoparticles is only limited on the surface of bulk g-C₃N₄.

In this article, a series of platinum nanoparticles-deposited carbon nitride nanotubes (Pt/C₃N₄ NTs) were prepared for the first time by a simple one-step solvothermal treatment strategy with Pt nanoparticles uniformly dispersed on the internal and external surface of C₃N₄ NTs. Ethanol was the lone structure-directing

* Corresponding author. Tel.: +86 791 83953373; fax: +86 791 83953373.
E-mail address: slou@hnu.edu.cn (S. Luo).

agent and reducing agent used in the preparation process. Therefore, the above method for Pt/C₃N₄ NTs preparation is a real “green” and economic synthesis method. The photocatalytic experiments showed that the visible-light photocatalytic activity of Pt/C₃N₄ NTs was significantly increased compared with that of bulk g-C₃N₄ in hydrogen evolution and *p*-chlorophenol degradation system. In addition, the activities of simultaneous hydrogen evolution with organic pollutant degradation were also tested using Pt/C₃N₄ NTs under representative organic pollutants (OPs) *p*-chlorophenol (PCP), *p*-nitrophenol (PNP), methylene blue (MB), or rhodamine B (RB) as electron donor conditions. Both hydrogen evolution and organic pollutant degradation reactions are based on the same photo-induced charge transfer process. However, the above photocatalytic reactions are performed usually by different photocatalysts under different experimental conditions because of the difference in their required charge transfer characteristics [24]; the organic pollutant degradation reaction originates from single-electron transfer under aerobic conditions whereas hydrogen evolution reaction is carried out by two-electron transfer in the absence of oxygen. Some organic pollutants of which redox potential is more negative than the valence band (VB) potential of TiO₂ can be used as an electron donor for hydrogen evolution reaction. So far, the photocatalytic system on simultaneous hydrogen evolution with organic pollutant degradation has been investigated by some researchers using TiO₂-based photocatalysts [25,26]. However, this special photocatalytic system has never been studied by using g-C₃N₄-based photocatalysts.

2. Experimental

2.1. Chemicals and reagents

Melamine (C₃H₆N₆, AR grade) was purchased from Tianjin Damao Chemical Reagent. Chloroplatinic acid (H₂PtCl₆·6H₂O, GR grade) was purchased from Sinopharm Chemical Reagent Co. Ltd. Triethylamine ((C₂H₅)₃N, AR grade, abbreviated TEA) was purchased from Shanghai Fine Chemical Technology Co. Ltd. *p*-Chlorophenol (C₆H₅ClO, GC grade, abbreviated PCP), *p*-nitrophenol (C₆H₅NO₃, GC grade, abbreviated PNP), methylene blue (C₁₆H₁₈ClN₃S·3H₂O, HPLC grade, abbreviated MB), and rhodamine B (C₂₈H₃₁ClN₂O₃, HPLC grade, abbreviated RB) were purchased from Aladdin Chemistry Co. Ltd. All chemicals were used without further purification. Double distilled water was used in the catalyst preparation and subsequent catalytic tests.

2.2. Preparation of Pt/C₃N₄ NTs by one-step solvothermal treatment

Pure g-C₃N₄ sample was prepared by directly calcining melamine in air. Typically, 50 g of melamine powder was put into a 100 mL alumina crucible with a cover. The crucible was heated to 250 °C from room temperature in a muffle furnace at a heating rate of 5 °C/min, and then continued heated to 550 °C at a heating rate of 10 °C/min. Keeping the temperature at 550 °C for 2 h, the yellow g-C₃N₄ sample was obtained after natural cooling.

Pt/C₃N₄ NTs was fabricated by one-step solvothermal treatment, with g-C₃N₄ and H₂PtCl₆·6H₂O as precursors. First, 1 g of g-C₃N₄ powder was uniformly dispersed into 15 mL ethanol using a 500 W ultrasonic crusher for 1 h. Subsequently, the desired amount of H₂PtCl₆·6H₂O (26.6, 53.2, 79.8, and 106.4 mg) was dissolved in 15 mL ethanol. The above H₂PtCl₆·6H₂O/ethanol solution was successively added in the above g-C₃N₄/ethanol suspension. After stirring the resulting mixture for 1 h at room temperature, the mixture was subject to solvothermal treatment at 150 °C for 24 h at a heat rate of 1 °C/min. The final products were obtained by drying

at 60 °C for 24 h and thermal treatment at 120 °C for 24 h, respectively, and denoted as Pt(x%)/C₃N₄ NTs, where x% represents Pt nanoparticles deposited mass percentage in the products.

For comparison, C₃N₄ NTs and Pt(2%)/TiO₂ samples were also prepared by the same method but in the absence of H₂PtCl₆·6H₂O precursor and use TiO₂ as a support. Pure TiO₂ was prepared by traditional sol-gel method and crystallizing at 450 °C for 5 h.

2.3. Characterizations

Transmission electron microscopy (TEM) images were recorded on a JEOL JEM-2010 transmission electron microscope at an accelerating voltage of 200 kV. Field emission scanning electron microscopy (FESEM) images were recorded using a Nova NanoSEM450 field emission scanning electron microscope. The chemical compositions and elemental mappings of the samples were determined by energy-dispersive X-ray spectrometer (EDX) equipped on FESEM. Nitrogen gas porosimetry measurements were performed on a Quantachrome NOVA 2000e surface area and porosity analyzer after the samples were outgassed under a vacuum at 70 °C for 20 min and 150 °C for 6 h. X-ray diffraction (XRD) patterns were obtained using a Panalytical X'Pert PRO diffractometer via Cu Kα radiation. Fourier transform infrared (FTIR) spectra were recorded on a Bruker VERTEX 70 FTIR apparatus. X-ray photoelectron spectra (XPS) was performed using a VG-ADES 400 instrument with an Mg Kα-ADES source at a residual gas pressure of less than 10^{−8} Pa. UV–visible/diffuse reflectance spectroscopy (UV-vis/DRS) was conducted using a Lambda 750S UV/VIS/NIR spectrometer. Photoluminescence (PL) measurements were carried out on a HITACHI F-7000 fluorescence spectrophotometer.

2.4. Photocurrent measurements

Photocurrent measurements were carried out using the conventional three electrode setup connected to an electrochemical station (CHI 630E, Shanghai Chenhua, China). In this electrochemical system, the prepared catalyst/Ti sheet was used as the working electrode; a Pt wire was used as the counter electrode and an Ag/AgCl electrode (saturated KCl) was used as the reference electrode. The electrolyte was 0.01 mol L^{−1} Na₂SO₄ aqueous solution (100 mL). A 300 W Xe lamp served as a light source. The measurements were carried out at a constant potential of +1.0 V to the working electrode.

2.5. Photocatalytic tests

2.5.1. Hydrogen evolution by using TEA as an electron donor

A PLS-SXE300 Xe lamp (300 W, Beijing PerfectLight Co. Ltd., China) served as the light source, and the output wavelength λ > 320 nm. The visible light irradiation was obtained by removing the UV irradiation from the lamp using a 420 nm cut filter, which can control the output wavelength λ > 420 nm. 100 mg of solid catalyst loaded with 3 wt% of Pt co-catalyst (for bulk g-C₃N₄ and C₃N₄ NTs only) and 100 mL of H₂O containing 10 vol% TEA were poured into a 300 mL quartz reactor. The above suspension was ultrasonicated for 10 min and stirred in dark for 1 h. Subsequently, the light source was switched on, and further stirring was applied. The temperature of the suspension was maintained at 35 ± 2 °C by circulation of water through an external cooling jacket. The generated hydrogen was *in situ* analyzed with a GC 7890-II TCD gas chromatograph (TECHCOMP) using an MS-5 A column, which was connected to the gas circulating line with argon carrier.

2.5.2. Photocatalytic degradation of aqueous PCP

100 mg of solid catalyst and 100 mL of PCP aqueous solution was poured into a 300 mL self-designed quartz reactor. The initial

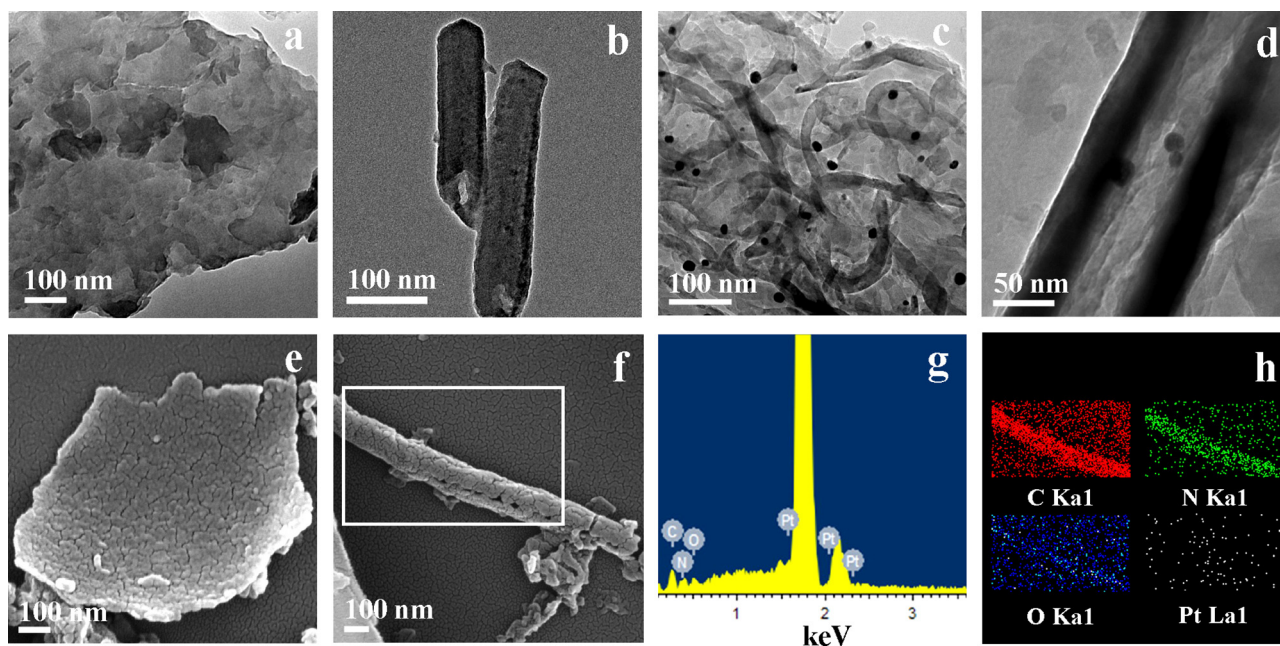


Fig. 1. TEM images of bulk g-C₃N₄ (a), C₃N₄ NTs (b), and Pt(2%)/C₃N₄ NTs (c and d) and FESEM images of bulk g-C₃N₄ (e) and Pt(2%)/C₃N₄ NTs (f). EDX spectrum (g) of Pt(2%)/C₃N₄ NTs and corresponding EDX elemental mappings (h) from selected area (f) for C, N, O, and Pt regions.

concentration of PCP is 20 mg L⁻¹. The suspension was ultrasonicated for 10 min and stirred in the dark until adsorption–desorption equilibrium. Subsequently, the light source was switched on, and further stirring was applied. The temperature of the suspension was maintained at 35 ± 2 °C by circulation of water through an external cooling jacket. At specific intervals of irradiation, fixed amounts of the reaction solution were extracted, centrifuged, and filtered. Changes in the PCP concentrations were analyzed using an Agilent 1100 series high-performance liquid chromatography.

2.5.3. Simultaneous hydrogen evolution with organic pollutant degradation

The initial hydrogen evolution system, that is 100 ml of H₂O containing 10 vol% TEA, was replaced by 100 ml of organic pollutant aqueous solution. The initial concentration of each organic pollutant is 20 mg L⁻¹. The adsorption–desorption equilibrium between organic pollutant and photocatalyst need to be reached before the start of hydrogen evolution reaction, and the saturated photocatalyst was separated and putted into a new reaction solution. Pt(2%)/C₃N₄ NTs sample was selected as a photocatalyst and the irradiation time continued for 24 h. Changes in the PCP and PNP concentrations were analyzed using an Agilent 1100 series high-performance liquid chromatography: C₁₈ column, UV detector (λ = 277 nm for PCP, λ = 318 nm for PNP), and acetonitrile/water (60/40, v/v) was used as a mobile phase at a flow rate of 1.0 mL/min. Changes in the MB and RB concentrations were analyzed using an UNICO UV-2000 spectrophotometer at λ = 664 and 554 nm, respectively.

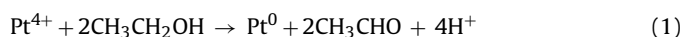
3. Results and discussion

3.1. Characterizations

3.1.1. Morphology and textural property

The morphology of bulk g-C₃N₄, C₃N₄ NTs, and Pt/C₃N₄ NTs (represented by Pt(2%)/C₃N₄ NTs) were revealed by TEM and FESEM observations (Fig. 1). As shown in the TEM image in Fig. 1a, bulk g-C₃N₄ has a graphite-like layered structure corresponding to the FESEM observation presented in Fig. 1e. As shown in Fig. 1b,

C₃N₄ NTs have an open end and hollowed tubular nanostructure. The inner and outer diameters of these two C₃N₄ NTs are approximately 60 and 80 nm, respectively, and the wall thickness is approximately 10 nm. This result indicates that the C₃N₄ NTs were successfully prepared through solvothermal treatment by using bulk g-C₃N₄ as a precursor. Some researchers have suggested that the tubular nanostructure reduced the charge imbalance caused by unsaturated or dangling bonds at the edges of the intermediate structure [27,28]. Other researchers have justified nanotube formation through an asymmetric chemical environment or mechanical stress [29,30]. We proposed that the tubular nanostructure was fabricated by the condensation of –OH on the surface of g-C₃N₄ nanosheets. Specifically, the g-C₃N₄ nanosheets were obtained by peeling off bulk g-C₃N₄ in ethanol using an ultrasonic crusher, and then the unbonded –NH₂ groups on the surface of g-C₃N₄ nanosheets were substituted with –OH groups of ethanol in the course of solvothermal reaction. As a result, the C₃N₄ NTs were constructed by the condensation of surface –OH on the g-C₃N₄ nanosheets. Similar result has been reported in our previous work [31]. The tubular nanostructures with different diameters were clearly observed in the TEM images of Pt(2%)/C₃N₄ NTs, as well as the sphere-like Pt nanoparticles of which average diameter is about 5 nm homogeneously dispersed on the inner and outer surface of C₃N₄ NTs (Fig. 1c and d). The average diameter of C₃N₄ NTs shown in Fig. 1c is approximately 30–40 nm, and most of the Pt nanoparticles are distributed on the outer surface of C₃N₄ NTs. The size of the individual C₃N₄ NTs shown in Fig. 1d is larger than those shown in Fig. 1c. The inner and outer diameters of this individual C₃N₄ NTs are about 50 and 100 nm, respectively. The above results suggest that Pt/C₃N₄ NTs were successfully prepared by one-step solvothermal treatment. The size of each C₃N₄ NTs cannot be controlled and determined by the size of a curly g-C₃N₄ nanosheets unit. In addition, Pt⁴⁺ can be reduced into metallic Pt under solvothermal treatment conditions. Formation of metallic Pt is attributed to the oxidation of ethanol under solvothermal treatment conditions (Eq. (1)). The similar result has been reported in our previous work [32].



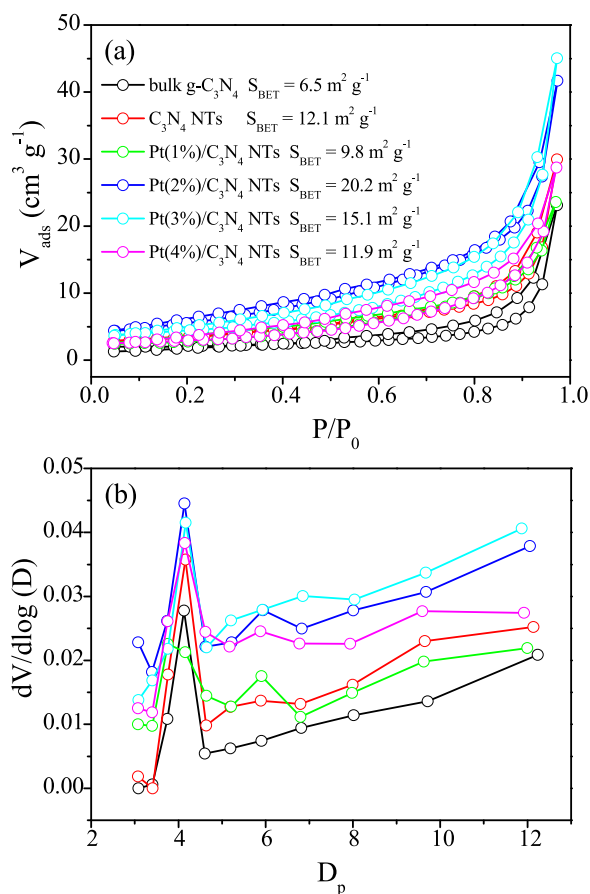


Fig. 2. Nitrogen gas sorption isotherms (a) and pore-size distribution curves (b) of as-prepared materials.

EDX spectrum and corresponding EDX elemental mappings from the selected area show that the C, N, O, and Pt elements exist in the Pt(2%)/C₃N₄ NTs, and Pt element is homogeneously distributed throughout the C₃N₄ NTs (Fig. 1f–h).

The textural property of bulk g-C₃N₄, C₃N₄ NTs, and Pt/C₃N₄ NTs was characterized by nitrogen gas porosity measurement (Fig. 2). As shown in the sorption isotherms shown in Fig. 2a, all of the tested materials exhibit type IV isotherms with H3 hysteresis loops indicating the mesoporosity of the materials regardless of their differences in morphology and Pt nanoparticles loading. The mesostructures of these materials are constructed by the secondary accumulation of the structural unit. The BET (Brunauer–Emmett–Teller) surface areas of C₃N₄ NTs and Pt/C₃N₄ NTs are larger than that of bulk g-C₃N₄ because of their tubular nanostructure with both exposed internal and external geometrical surfaces. In addition, the BET surface areas increase with increasing the Pt nanoparticles loading from 1% to 2%; however, the BET surface areas gradually decrease with further increasing the Pt nanoparticles loading to 3% and 4%. This result suggests that C₃N₄ NTs are partially blocked after excessive amount of Pt nanoparticles is introduced. The BJH (Barrett–Joyner–Halenda) pore-size distribution curves reveal that all of the tested materials exhibit a narrow peak centered at 4.1 nm, which is attributed to the released NH₃ that act as soft-templates during the course of melamine polycondensation (Fig. 2b). The broad pore size distribution peaks in C₃N₄ NTs and Pt/C₃N₄ NTs samples originate from the open end of C₃N₄ NTs and the void space between tubular nanostructures.

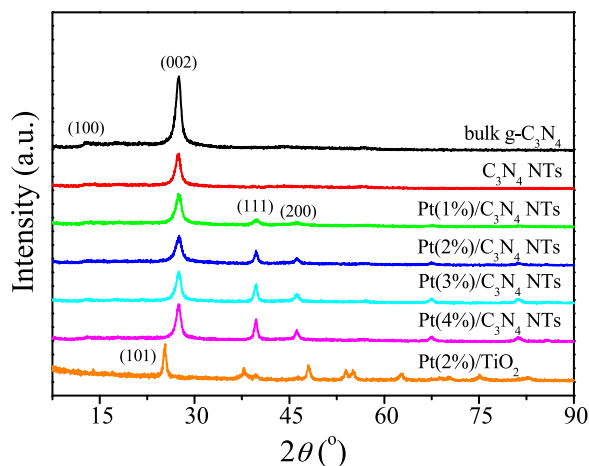


Fig. 3. XRD patterns of as-prepared materials.

3.1.2. Compositional and structural information

The phase structures of bulk g-C₃N₄, C₃N₄ NTs, Pt/C₃N₄ NTs, and Pt/TiO₂ were characterized by XRD analysis (Fig. 3). The results revealed that bulk g-C₃N₄ exhibits a typical (002) interlayer-stacking peak at 27.5° which corresponds to an interlayer distance of $d = 0.33$ nm, while the (100) peak at 12.6° represents in-plane structural packing motif with a period of 0.675 nm. As for the C₃N₄ NTs and Pt/C₃N₄ NTs samples, the diffraction intensity of (002) peak became weak, demonstrating that the content of layered structure was reduced after ultrasonic crashing and solvothermal treatment. The diffraction peaks at 39.7° and 46.1° for Pt nanoparticles-deposited samples were assigned to (111) and (200) planes of Pt nanoparticles in face-centered cubic structure. This result further proves that Pt⁴⁺ was successfully reduced and aggregated into metallic Pt nanoparticles under solvothermal treatment conditions. In addition, the characteristic diffraction peak of Pt(2%)/TiO₂ sample at 25.2° (101) demonstrates its anatase crystal phase structure (JCPDS No. 21-1272).

Fig. 4 shows the FTIR spectra of bulk g-C₃N₄, C₃N₄ NTs, and Pt/C₃N₄ NTs. For all the tested materials, a series of peaks found in the range of 1700–1000 cm^{−1} is attributed to the stretching modes like C–N and C=N in the CN heterocycles. The sharp peak at 806.7 cm^{−1} is the typical bending vibration of s-triazine units. The broad absorption peaks located in the range of 3400–2800 cm^{−1} originates from the stretching vibrational modes of primary (–NH₂)

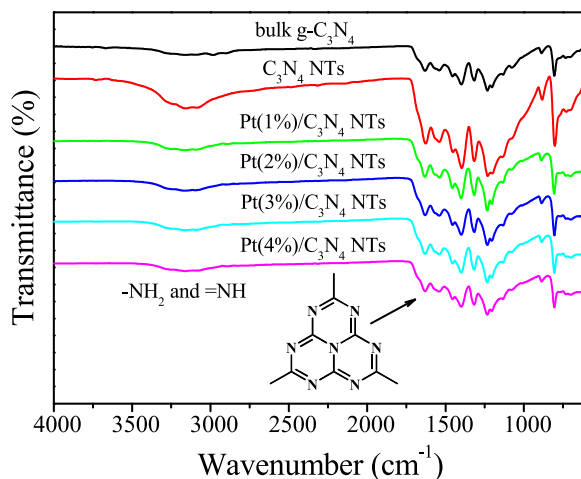


Fig. 4. FTIR spectra of as-prepared materials.

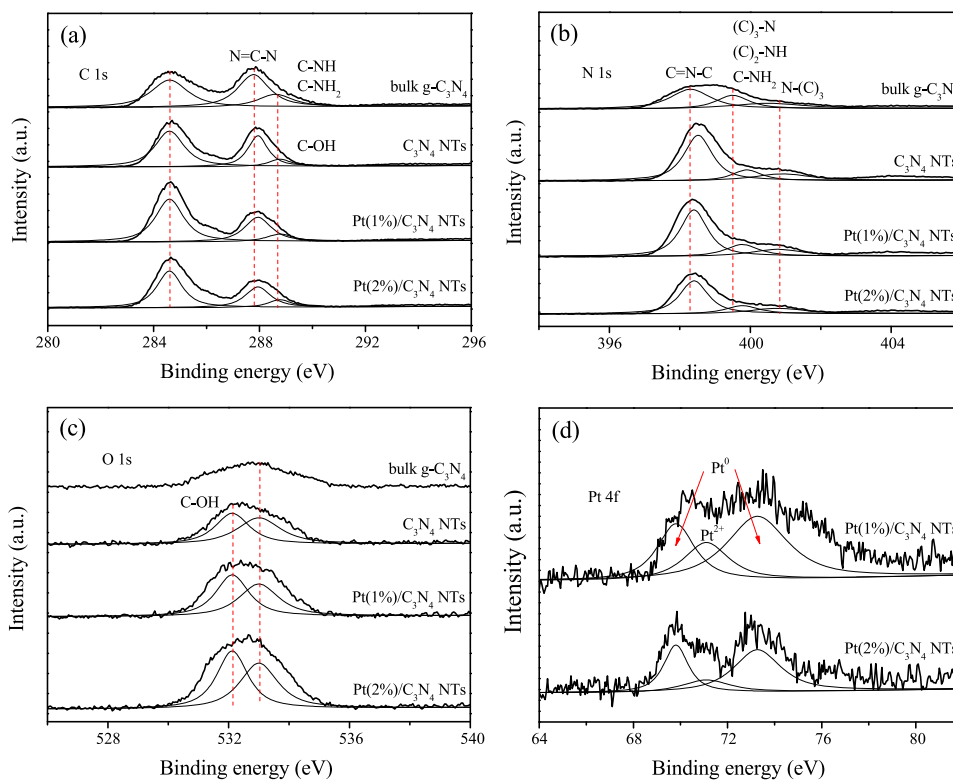


Fig. 5. High-resolution XPS of as-prepared materials in the C 1s (a), N 1s (b), O 1s (c), and Pt 4f (d) binding energy regions.

and secondary (=NH) amines. Clearly, the FTIR spectra of C_3N_4 NTs and Pt/ C_3N_4 NTs are similar to that of bulk g- C_3N_4 , indicating that C_3N_4 NTs and Pt/ C_3N_4 NTs keep the same chemical structure as bulk g- C_3N_4 after solvothermal treatment. The C_3N_4 NTs demonstrate a stronger FTIR mode compare with bulk g- C_3N_4 owing to their more exposed surface functional groups. However, for the Pt/ C_3N_4 NTs samples, the FTIR mode was weakened after depositing Pt nanoparticles on the surface of C_3N_4 NTs because the surface functional groups on the C_3N_4 NTs were covered by deposited Pt nanoparticles.

The surface composition and chemical state of the constituent elements of bulk g- C_3N_4 , C_3N_4 NTs, and Pt/ C_3N_4 NTs were characterized by a high-resolution XPS probe technique (Fig. 5). As shown in Fig. 5a, the peak of bulk g- C_3N_4 in C 1s binding energy regions centered at 284.6 eV is typically assigned to C–C and/or C=C, which originates from the adventitious reference carbon on the surface [33]. The peak centered at 287.8 eV originates from sp^2 C atoms bonded to N in an aromatic ring (N=C–N), whereas the peak centered at 288.7 eV is assigned to sp^2 C atoms in the aromatic ring attached to the primary and secondary amines (C–NH₂, C–NH). The peaks of C_3N_4 NTs and Pt/ C_3N_4 NTs which originate from sp^2 C atoms shift to a higher binding energy direction than that of bulk g- C_3N_4 sample, indicating that the –NH₂ groups within bulk g- C_3N_4 has been substituted with the –OH groups to form a C–OH species after solvothermal treatment. The original, electronic, sp^2 C atom environment is perturbed by the –OH groups. The results of high-resolution XPS with respect to the N 1s binding energy regions support the high-resolution XPS analysis of the C 1s binding energy regions described above (Fig. 5b). The peak of bulk g- C_3N_4 centered at 398.3 eV is assigned to sp^2 -hybridized aromatic nitrogen atoms bonded to carbon atoms (C=N–C). The peak centered at 399.5 eV is related to either tertiary nitrogen (C)₃–N groups linking structural motifs (C₆N₇) or amino groups carrying hydrogen ((C)₂–NH,

C–NH₂) in connection with structural defects and incomplete condensation. A weak peak at 400.8 eV corresponds to nitrogen atoms bonded to three carbon atoms in the aromatic cycles. For the C_3N_4 NTs and Pt/ C_3N_4 NTs samples, the peak centered at 399.5 eV weakens more compared with that of bulk g- C_3N_4 because of the missing –NH₂ group. The shift in the N 1s binding energy compared with that of bulk g- C_3N_4 is attributed to –OH group substitution. As shown in Fig. 5c, bulk g- C_3N_4 exhibits O 1s binding energy region centered at 533.0 eV, ascribed to the adsorbed water. After solvothermal treatment, the O 1s peaks of C_3N_4 NTs and Pt/ C_3N_4 NTs centered at 533.0 eV were increased and removed to the lower binding energy direction compare with that of bulk g- C_3N_4 , attributed to the formation of C–OH species at 532.1 eV. Fig. 5d presents the high-resolution XPS of Pt/ C_3N_4 NTs in the Pt 4f binding energy region. The main peaks at 69.8 and 73.3 eV originated from metallic Pt (Pt⁰), and the weak peak at 71.1 eV is the oxidized form of Pt (Pt²⁺) which originated from incompletely reductive Pt⁴⁺ precursor.

3.1.3. Optical and electronic properties

The light absorption properties of bulk g- C_3N_4 , C_3N_4 NTs, Pt/ C_3N_4 NTs, and Pt/TiO₂ were studied by UV–vis/DRS (Fig. 6). Bulk g- C_3N_4 shows a typical semiconductor absorption within the region of 200–450 nm, which originates from the charge-transfer response from VB populated by N 2p orbit to the conduction band (CB) formed by C 2p orbit. The light absorption abilities of C_3N_4 NTs and Pt/ C_3N_4 NTs were increased compared with that of g- C_3N_4 in the range of 200–450 nm owing to their nano-size effect, because both C_3N_4 NTs and Pt nanoparticles are more beneficial than their corresponding bulk structures for multiple reflections of incident light. Therefore, the light absorption abilities of Pt/ C_3N_4 NTs were gradually increased in the range of 200–450 nm with increasing Pt nanoparticles loading

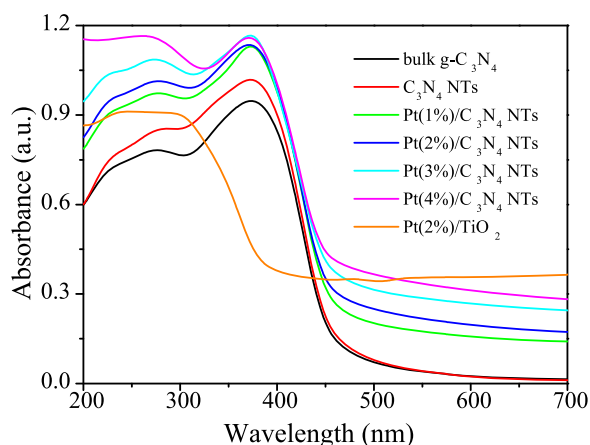


Fig. 6. UV-vis/DRS of as-prepared materials.

from 0% to 4%. The increased light absorption abilities of Pt/C₃N₄ NTs in the range of 450–700 nm are attributed to the decrease in reflectivity evidenced by the dark gray color of the sample [34]. In addition, Pt(2%)/TiO₂ sample shows a strong light response within the range of 200–400 nm, which can be attributed to the electron transition from VB (O 2p) to CB (Ti 3d). The weak light absorption of Pt(2%)/TiO₂ in the range of 400–700 nm are also attributed to the decrease in reflectivity evidenced by the dark gray color of the sample. The UV-vis/DRS result of Pt(2%)/TiO₂ sample implies that Pt(2%)/TiO₂ cannot be excited by $\lambda > 420$ nm visible-light irradiation.

The photocatalytic quantum efficiencies of bulk g-C₃N₄, C₃N₄ NTs, and Pt/C₃N₄ NTs were studied by PL measurements and photoelectrochemistry tests (Fig. 7). As shown in Fig. 7a, bulk g-C₃N₄ exhibits luminescence in a broad range (400–600 nm) and is centered at ca. 450 nm under room temperature with an excitation wavelength of 330 nm. This finding suggests that photo-induced

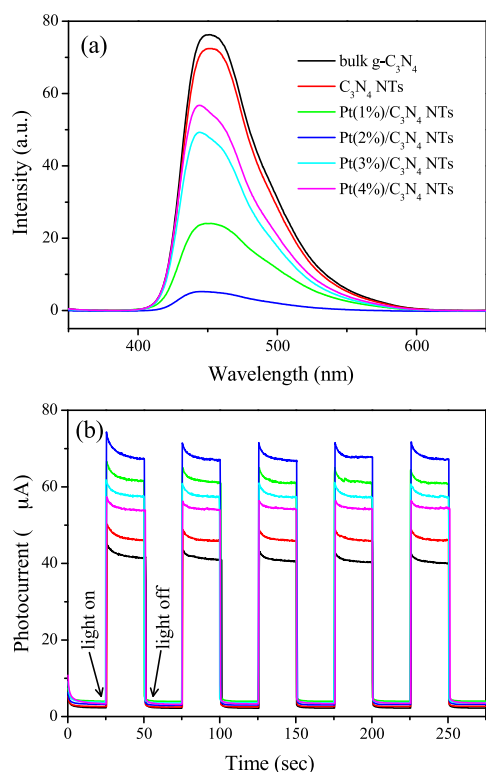


Fig. 7. PL spectra (a) and photocurrent responses (b) of as-prepared materials.

$e^- - h^+$ pairs are generated and recombined within the bulk g-C₃N₄. The PL intensities of C₃N₄ NTs and Pt/C₃N₄ NTs obviously decreased compared with that of bulk g-C₃N₄, suggesting that the recombination rate of photogenerated $e^- - h^+$ pairs in the C₃N₄ NTs and Pt/C₃N₄ NTs have decelerated. The above result suggests that efficient separation, transportation, and capture of the photogenerated carriers are realized after the formation of tubular nanostructure and deposition of Pt nanoparticles. In addition, the PL intensities of Pt/C₃N₄ NTs gradually decrease with increasing Pt nanoparticles loading from 0% to 2%. However, the PL intensities of Pt/C₃N₄ NTs gradually increase with the further ascent of Pt nanoparticles loading to 3% and 4%. This result suggests that Pt/C₃N₄ NTs with high Pt nanoparticles loadings exhibit weak photogenerated carriers transfer capability because new $e^- - h^+$ recombination centers were fabricated by the aggregation of excessive Pt nanoparticles. Sharp increases in photocurrent responses can be observed in all the tested working electrodes once pulse Xe lamp irradiation is activated, as displayed by the photocurrent–time (*I*–*t*) curves shown in Fig. 7b. The generated photocurrents are reproducible and stable during five intermittent on–off irradiation cycles. The prompt increase in photocurrent response from the light-off to the light-on state is ascribed to the quick separation and transportation of photogenerated electrons on the surfaces of working electrodes. C₃N₄ NTs exhibit higher photocurrent response than bulk g-C₃N₄ and the photocurrent response of Pt/C₃N₄ NTs is higher than that of C₃N₄ NTs. The photocurrent responses of Pt/C₃N₄ NTs gradually increase with increasing the Pt nanoparticles loading from 0% to 2%, but the photocurrent responses gradually decline upon increase of Pt nanoparticles loading to 3% and 4%. The results of photoelectrochemical experiment are consistent with the PL measurements described above, indicating that tubular nanostructure and deposited Pt nanoparticles can effectively slow down the recombination rate of photogenerated $e^- - h^+$ pairs. The declined photocurrent responses of Pt(3%)/C₃N₄ NTs and Pt(4%)/C₃N₄ NTs samples are attributed to the new $e^- - h^+$ recombination centers induced as a result of the aggregation of excessive Pt nanoparticles.

3.2. Photocatalytic tests

3.2.1. Hydrogen evolution from water-splitting by using TEA as an electron donor

The photocatalytic activities of Pt/C₃N₄ NTs and Pt/TiO₂ for hydrogen evolution from water-splitting were evaluated in 10 vol% TEA aqueous solution under $\lambda > 420$ nm visible-light irradiation without any co-catalyst. However, no hydrogen was detected in the absence of a co-catalyst for the bulk g-C₃N₄ and C₃N₄ NTs samples. Therefore, the hydrogen evolution reactions by bulk g-C₃N₄ and C₃N₄ NTs were carried out in the presence of 3 wt% Pt nanoparticles co-catalyst. As seen in Fig. 8a, no hydrogen was detected by using Pt(2%)/TiO₂ sample as a photocatalyst due to the lack of $\lambda > 420$ nm visible-light response of Pt(2%)/TiO₂. In addition, the hydrogen evolution efficiency is low by using methanol as an electron donor due to the poor electron-donating ability of methanol. The photocatalytic activity of C₃N₄ NTs is higher than that of bulk g-C₃N₄, and the photocatalytic activities of Pt/C₃N₄ NTs with suitable Pt nanoparticles loadings are higher than that of C₃N₄ NTs. The photocatalytic activities of the as-prepared materials followed the order of Pt(2%)/TiO₂ < bulk g-C₃N₄ < Pt(2%)/C₃N₄ NTs (methanol) < Pt(1%)/C₃N₄ NTs < C₃N₄ NTs < Pt(4%)/C₃N₄ NTs < Pt(3%)/C₃N₄ NTs < Pt(2%)/C₃N₄ NTs for hydrogen evolution from water-splitting. Pt(2%)/C₃N₄ NTs sample is the most photoactive photocatalyst among all the tested materials, exhibiting hydrogen evolution efficiency of 13.5 $\mu\text{mol/h}$. The nitrogen leak test was performed by using Pt(2%)/C₃N₄ NTs as a photocatalyst and TEA or methanol as an electron donor. Nitrogen test result shows that there is no nitrogen leak in the hydrogen

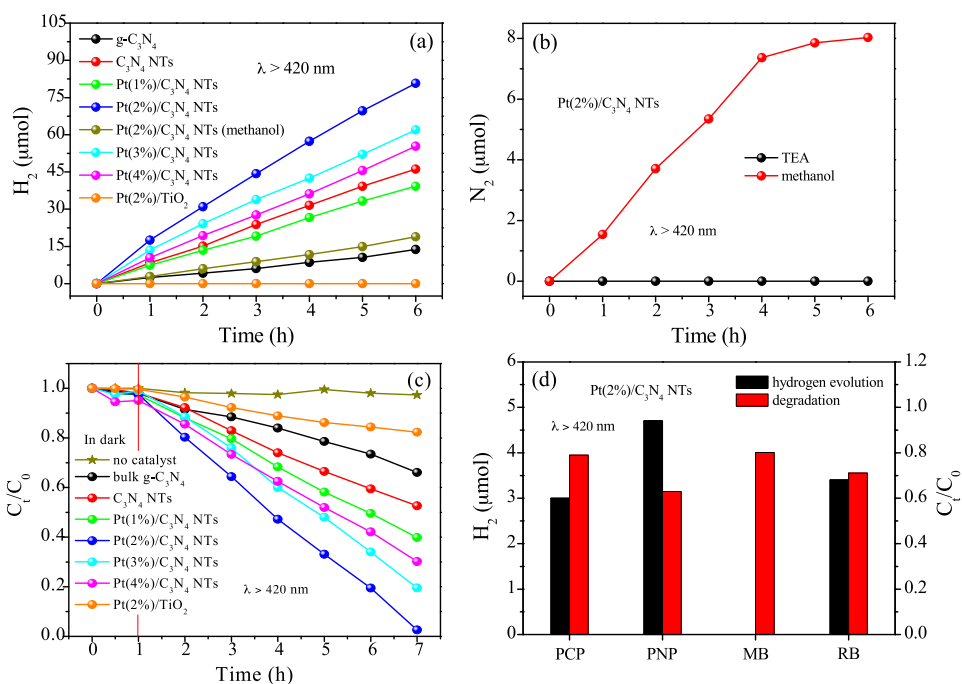


Fig. 8. Visible-light photocatalytic activities of as-prepared materials in three different systems: hydrogen evolution from water-splitting using TEA as an electron donor (a) and nitrogen leak test during the hydrogen evolution process by using TEA or methanol as an electron donor (b); photocatalytic degradation of aqueous PCP (c); simultaneous hydrogen evolution with organic pollutant degradation (d).

evolution process by using TEA as an electron donor; however, about 8 μmol of nitrogen was detected after 6 h visible-light irradiation by using methanol as an electron donor (Fig. 8b). This result suggests that about 0.37 wt% of lattice N^{3-} in the photocatalyst was oxidized by photogenerated holes during the hydrogen evolution process because of the poor electron-donating ability of methanol.

The efficient photocatalytic activity of Pt/C_3N_4 NTs prepared through one-step solvothermal treatment for hydrogen evolution from water-splitting is primarily attributed to the following three reasons: first, the fabrication of tubular nanostructure is important in enhancing the photocatalytic activity of bulk $g-C_3N_4$. On the one hand, the tubular nanostructure can increase the number of active sites and reduce the mass transfer resistance in the photocatalytic reaction process; guest species such as H_2O molecules, electron donors, and co-catalysts can easily access the active sites on the inner and outer surface of C_3N_4 NTs. Guest species can also be efficiently transported throughout the tubular photocatalyst, and thereby the reaction is not limited to the photocatalyst surface. On the other hand, a tubular nanostructure can also reduce the probability of $e^- - h^+$ pair recombination by improving photogenerated carriers transfer capability, thereby prolonging charge lifespan and transferring photogenerated charges to the H_2O molecules. Therefore, the photocatalytic activity of C_3N_4 NTs is obviously higher than that of bulk $g-C_3N_4$ under the same experimental conditions. Second, the deposited Pt nanoparticles on the surface of C_3N_4 NTs can significantly enhance the photocatalytic quantum efficiency because of the strong electron acceptability of Pt nanoparticles. Therefore, the photocatalytic activities of Pt/C_3N_4 NTs are enhanced with increasing Pt nanoparticles loading from 1% to 2%. However, the photocatalytic activity of Pt/C_3N_4 NTs gradually declines with increasing the Pt nanoparticles loading further to 3% and 4% because of the construction of new $e^- - h^+$ recombination centers that lower the photocatalytic quantum efficiency of Pt/C_3N_4 NTs. Third, the high light-utilization efficiency of Pt/C_3N_4 NTs has a positive effect on photocatalytic activity because it favors increased production of photogenerated electrons and holes under similar

visible-light irradiation. In addition, the photocatalytic activity of $Pt(3\%)/C_3N_4$ NTs is higher than that of C_3N_4 NTs under the similar Pt nanoparticles loading condition. This result illustrates that the solvothermal reduction strategy is more beneficial for Pt nanoparticles distribution in the C_3N_4 NTs than traditional photoreduction method. $Pt(1\%)/C_3N_4$ NTs exhibits the lowest photocatalytic activity among four tested Pt/C_3N_4 NTs samples because of its low light-utilization efficiency and small BET surface area with less active sites, even though its photocatalytic quantum efficiency is higher than $Pt(3\%)/C_3N_4$ NTs and $Pt(4\%)/C_3N_4$ NTs.

3.2.2. Photocatalytic degradation of aqueous PCP

The visible-light photocatalytic activity of bulk $g-C_3N_4$, C_3N_4 NTs, Pt/C_3N_4 NTs, and Pt/TiO_2 toward PCP degradation was conducted in an aqueous solution containing oxygen molecules from dissolved air. As shown in Fig. 8c, the results of the direct photodegradation experiment indicate that the change in PCP concentration in the reaction system is negligible under visible-light irradiation for 6 h. The adsorption test results show that the adsorption-desorption equilibrium was reached prior to Xe lamp irradiation. The photocatalytic test for aqueous PCP degradation obtained similar result with hydrogen evolution from water-splitting: the photocatalytic activity of $Pt(2\%)/TiO_2$ is negligible for aqueous PCP degradation because of the lack of $\lambda > 420$ nm visible-light response. The photocatalytic activity of C_3N_4 NTs is higher than that of bulk $g-C_3N_4$, and the photocatalytic activity of Pt/C_3N_4 NTs is higher than that of C_3N_4 NTs. The photocatalytic activity of Pt/C_3N_4 NTs is gradually enhanced with increasing Pt nanoparticles loading from 0% to 2%, whereas the photocatalytic activity of Pt/C_3N_4 NTs gradually declines with further increased Pt nanoparticles loading to 3% and 4%. The photocatalytic activities of the as-prepared materials followed the order of $Pt(2\%)/TiO_2 < bulk\ g-C_3N_4 < C_3N_4\ NTs < Pt(1\%)/C_3N_4\ NTs < Pt(4\%)/C_3N_4\ NTs < Pt(3\%)/C_3N_4\ NTs < Pt(2\%)/C_3N_4\ NTs$ for aqueous PCP degradation. $Pt(2\%)/C_3N_4$ NTs is the most photoactive photocatalyst among all the tested materials with PCP degraded

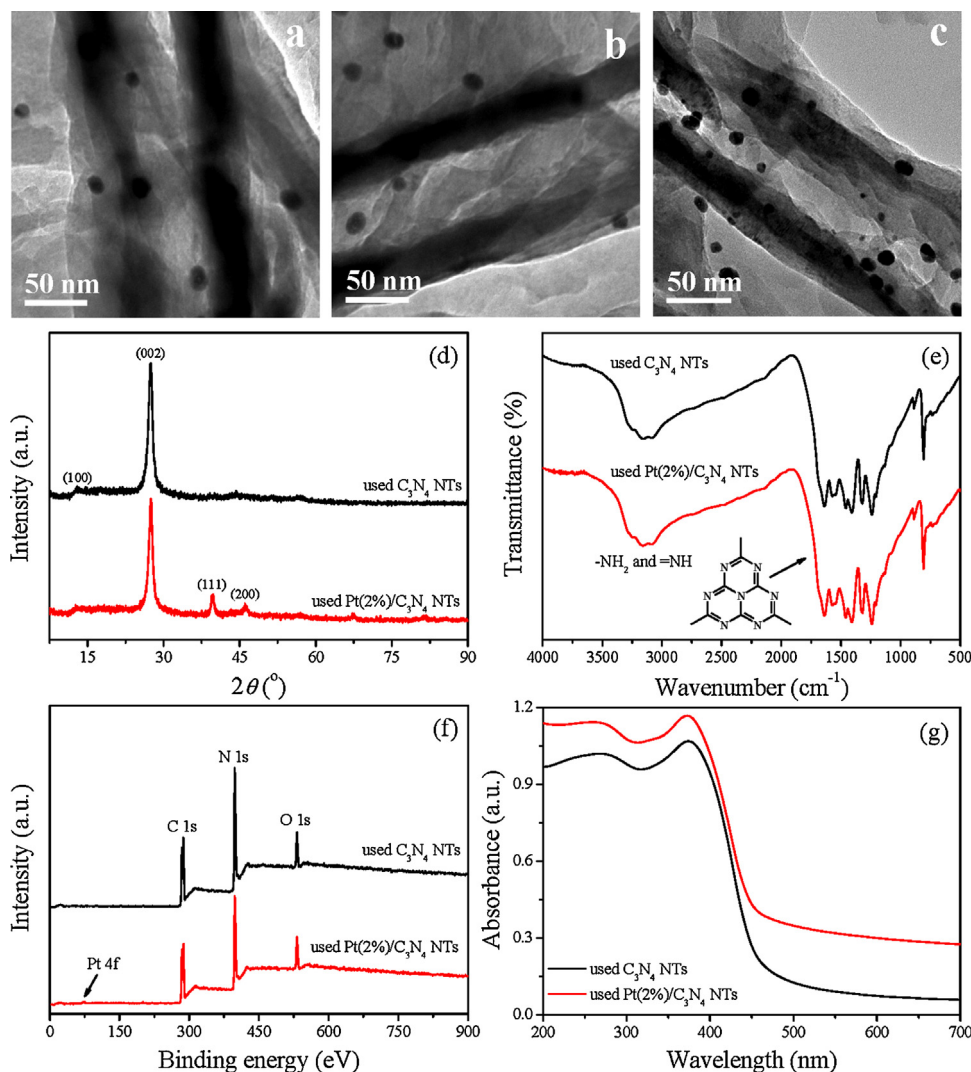


Fig. 9. TEM images of the used Pt(2%)/C₃N₄ NTs (a–c); and XRD patterns (d), FTIR spectra (e), XPS spectra (f), and UV-vis/DRS (g) of the used C₃N₄ NTs and Pt(2%)/C₃N₄ NTs after photocatalytic degradation reaction.

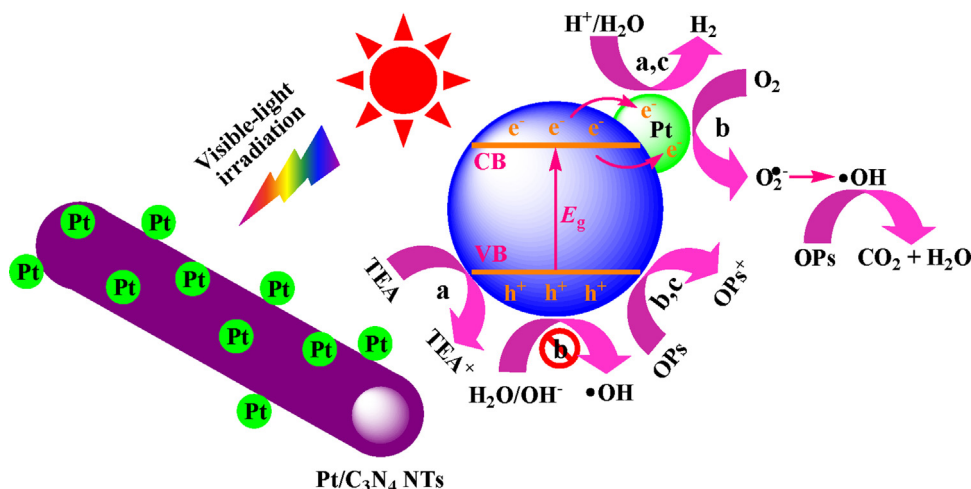
completely after 6 h visible-light irradiation. The efficient visible-light photocatalytic activity of as-prepared Pt/C₃N₄ NTs for aqueous PCP degradation is attributed to their high mass transfer capability, more exposed active sites, increased quantum efficiency, and enhanced visible-light utilization. The characterization results of the used C₃N₄ NTs and Pt(2%)/C₃N₄ NTs samples after photocatalytic degradation reaction are shown in Fig. 9. Through analysis of the results it is found that the morphology of Pt(2%)/C₃N₄ NTs and the phase and chemical structure, surface composition as well as light absorption property of C₃N₄ NTs and Pt(2%)/C₃N₄ NTs remain intact after the photocatalytic reaction.

3.2.3. Simultaneous hydrogen evolution with organic pollutant degradation

The simultaneous hydrogen evolution with organic pollutant degradation experiment was performed by using Pt(2%)/C₃N₄ NTs as a photocatalyst and representative organic pollutants PCP, PNP, MB, or RB as electron donors. The result shown in Fig. 8d indicates that both hydrogen evolution and photocatalytic degradation activities of Pt(2%)/C₃N₄ NTs decreased in the current photocatalytic system. No hydrogen was detected when MB was selected as an electron donor. Obviously, the photocatalytic activity of Pt(2%)/C₃N₄ NTs for hydrogen evolution and degradation simultaneously increased or decreased when PCP, PNP, or RB is used

as an electron donor; the Pt(2%)/C₃N₄ NTs photocatalyst shows the highest activity for hydrogen evolution and degradation when PNP was used as an electron donor, and it exhibits the lowest activity for hydrogen evolution and degradation when PCP was used as an electron donor.

The degraded photocatalytic activity of Pt(2%)/C₃N₄ NTs toward hydrogen evolution and degradation in the current system is attributed to the following reasons: first, the hydrogen evolution reaction is carried out via two-electron transfer in the absence of oxygen. The recombination of hydrogen and oxygen can significantly reduce the yield of hydrogen evolution reaction. The excess amount of electron donor was usually used for irreversibly consuming photo-induced h^+ , $\cdot OH$, and oxygen in the traditional hydrogen evolution system. Therefore, the electron donor used for hydrogen evolution usually exhibits a strong electron-donating ability. Some organic pollutants can be used as electron donor if their redox potential is more negative than the VB potential of the semiconductor photocatalyst. However, the organic pollutants typically have stable chemical structures and poor electron-donating ability. Therefore, the photocatalytic activity of Pt(2%)/C₃N₄ NTs for hydrogen evolution is low when representative organic pollutants PCP, PNP, or RB are used as electron donors. In addition, the reduction potential of MB cation (1.66 V vs. NHE) is more positive than the VB potential of g-C₃N₄ (1.4 V vs. NHE) [35]; therefore there is



Scheme 1. Separation and transportation of photoinduced charge carriers in Pt/C₃N₄ NTs system under visible-light irradiation: hydrogen evolution from water-splitting using TEA as an electron donor (a); photocatalytic degradation of aqueous PCP (b); simultaneous hydrogen evolution with organic pollutant degradation (c).

no hydrogen generated when MB is used as an electron donor in the current system. The degraded concentration of MB is attributed to the decolorization reaction in acidic environment rather than the oxidation effect of photogenerated holes. Second, the photocatalysis for organic pollutant degradation is initiated by single electron transfer under aerated conditions. The organic pollutant is degraded in water as a result of the oxidation of $\bullet\text{OH}$ generated by $\text{O}_2^{\bullet-}$ and h^+ reacting with water. In our previous work, it is found that the VB potential of g-C₃N₄ is more negative than the redox potential of $\text{OH}^-/\bullet\text{OH}$ (1.99 V vs. NHE) [36]; therefore the photogenerated holes cannot directly oxidize OH^- to $\bullet\text{OH}$ in the g-C₃N₄-based photocatalytic system. The generation of $\bullet\text{OH}$ only relies on the reaction between $\text{O}_2^{\bullet-}$ and water, and the oxidizing effect of photogenerated holes was displayed by directly capturing the electron of the organic pollutant. The oxidation of organic pollutant only relies on captured electron from organic pollutant by photogenerated holes in the absence of oxygen. Therefore, the photocatalytic activity of Pt(2%)/C₃N₄ NTs is low for organic pollutant degradation in the current system. In addition, the organic pollutant with relatively strong electron-donating ability is prone to be oxidized by photogenerated holes, whereas the organic pollutant with relatively poor electron-donating ability is hard to be oxidized by photogenerated holes. Therefore, the photocatalytic activity of Pt(2%)/C₃N₄ NTs for hydrogen evolution and degradation is simultaneously increased or decreased when PCP, PNP, or RB is used as an electron donor. The above-discussed photocatalytic mechanisms in three different systems are briefly shown in Scheme 1.

4. Conclusions

A series of Pt/C₃N₄ NTs materials was successfully prepared by a simple one-step solvothermal treatment strategy, with bulk g-C₃N₄ and H₂PtCl₆·6H₂O as precursors. The efficient photocatalytic activity of as-prepared Pt/C₃N₄ NTs for hydrogen evolution from water-splitting and aqueous PCP degradation under visible-light irradiation is attributed to their unique tubular nanostructure and the synergic effect of Pt nanoparticles. In the simultaneous hydrogen evolution with organic pollutant degradation system, the simultaneous decrease in the photocatalytic activity of Pt/C₃N₄ NTs for hydrogen evolution and degradation reactions are due to the poor electron-donating ability of organic pollutants and weak oxidation capacity of photogenerated holes in the anoxic environment.

Acknowledgements

This work was financially supported by the National Natural Science Foundation of China (51208248, 51238002, 51272099, 51238001, 51278092, 21366024, 21165013); Science and Technology Major Bidding Project of Jiangxi Province, China (No. Gan Ke Fa Ji Zi [2010] 217); Youth Science Foundation of Jiangxi Province, China (20114BAB213015); Natural Science Foundation of Jiangxi Provincial Department of Education, China (GJJ12456, GJJ14515).

References

- [1] X. Chen, S.S. Mao, *Chem. Rev.* 107 (2007) 2891–2959.
- [2] X. Chen, S. Shen, L. Guo, S.S. Mao, *Chem. Rev.* 110 (2010) 6503–6570.
- [3] M. Wang, J. Iocozia, L. Sun, C. Lin, Z. Lin, *Energy Environ. Sci.* 7 (2014) 2182–2202.
- [4] Q. Wang, J. Li, Y. Bai, J. Lian, H. Huang, Z. Li, Z. Lei, W. Shanguan, *Green Chem.* 16 (2014) 2728–2735.
- [5] Z. Zhang, C. Shao, X. Li, Y. Sun, M. Zhang, J. Mu, P. Zhang, Z. Guo, Y. Liu, *Nanoscale* 5 (2013) 606–618.
- [6] S. Liu, J. Yu, M. Jaroniec, *Chem. Mater.* 23 (2011) 4085–4093.
- [7] D.K. Padhi, K. Parida, J. Mater. Chem. A 2 (2014) 10300–10312.
- [8] H. Zhou, L. Ding, T. Fan, J. Ding, D. Zhang, Q. Guo, *Appl. Catal. B: Environ.* 147 (2014) 221–228.
- [9] J. Sheng, X. Li, Y. Xu, *ACS Catal.* 4 (2014) 732–737.
- [10] M. Tahir, N.A.S. Amin, *Appl. Catal. B: Environ.* 142–143 (2013) 512–522.
- [11] X. Wang, K. Maeda, A. Thomas, K. Takanabe, G. Xin, J.M. Carlsson, K. Domen, M. Antonietti, *Nat. Mater.* 8 (2009) 76–80.
- [12] X. Wang, K. Maeda, X. Chen, K. Takanabe, K. Domen, Y. Hou, X. Fu, M. Antonietti, *J. Am. Chem. Soc.* 131 (2009) 1680–1681.
- [13] T. Li, L. Zhao, Y. He, J. Cai, M. Luo, J. Lin, *Appl. Catal. B: Environ.* 129 (2013) 255–263.
- [14] L. Ge, C. Han, J. Liu, *Appl. Catal. B: Environ.* 108–109 (2011) 100–107.
- [15] F. Su, S.C. Mathew, G. Lipner, X. Fu, M. Antonietti, S. Blechert, X. Wang, *J. Am. Chem. Soc.* 132 (2010) 16299–16301.
- [16] L. Ge, C. Han, J. Liu, *J. Mater. Chem.* 22 (2012) 11843–11850.
- [17] S. Kumar, T. Surendar, A. Baruah, V. Shanker, *J. Mater. Chem. A* 1 (2013) 5333–5340.
- [18] S. Yang, Y. Gong, J. Zhang, L. Zhan, L. Ma, Z. Fang, R. Vajtai, X. Wang, P.M. Ajayan, *Adv. Mater.* 25 (2013) 2452–2456.
- [19] J. Zhang, F. Guo, X. Wang, *Adv. Funct. Mater.* 23 (2013) 3008–3014.
- [20] X.H. Li, X. Wang, M. Antonietti, *ACS Catal.* 2 (2012) 2082–2086.
- [21] K.K. Datta, B.V. Reddy, K. Ariga, A. Vinu, *Angew. Chem. Int. Ed.* 49 (2010) 5961–5965.
- [22] L. Ge, C. Han, J. Liu, Y. Li, *Appl. Catal. A: Gen.* 409–410 (2011) 215–222.
- [23] J. Liu, Y. Zhang, L. Lu, G. Wu, W. Chen, *Chem. Commun.* 48 (2012) 8826–8828.
- [24] J. Kim, D. Monllor-Satoca, W. Choi, *Energy Environ. Sci.* 5 (2012) 7647–7656.
- [25] J. Kim, W. Choi, *Energy Environ. Sci.* 3 (2010) 1042–1045.
- [26] V.M. Daskalaki, M. Antoniadou, G.L. Puma, D.I. Kondarides, P. Lianos, *Environ. Sci. Technol.* 44 (2010) 7200–7205.
- [27] P. Liu, H. Zhang, H. Liu, Y. Wang, X. Yao, G. Zhu, S. Zhang, H. Zhao, *J. Am. Chem. Soc.* 133 (2011) 19032–19035.
- [28] R.D. White, D.V. Bavykin, F.C. Walsh, *J. Mater. Chem. A* 1 (2013) 548–556.

- [29] D.V. Bavykin, V.N. Parmon, A.A. Lapkin, F.C. Walsh, J. Mater. Chem. 14 (2004) 3370–3377.
- [30] M.D. Hernández-Alonso, S. García-Rodríguez, B. Sánchez, J.M. Coronado, *Nanoscale* 3 (2011) 2233–2240.
- [31] K. Li, L. Yan, Z. Zeng, S. Luo, X. Luo, X. Liu, H. Guo, Y. Guo, *Appl. Catal. B: Environ.* 156–157 (2014) 141–152.
- [32] X. Yang, Y. Wang, L. Xu, X. Yu, Y. Guo, *J. Phys. Chem. C* 112 (2008) 11481–11489.
- [33] S. Zhang, Y. Yang, Y. Guo, W. Guo, M. Wang, Y. Guo, M. Huo, J. Hazard. Mater. 261 (2013) 235–245.
- [34] J.J. Murcia, J.A. Navío, M.C. Hidalgo, *Appl. Catal. B: Environ.* 126 (2012) 76–85.
- [35] M.M. Khan, J. Lee, M.H. Cho, *J. Ind. Eng. Chem.* 20 (2014) 1584–1590.
- [36] Y. Yang, Y. Guo, F. Liu, X. Yuan, Y. Guo, S. Zhang, W. Guo, M. Huo, *Appl. Catal. B: Environ.* 142–143 (2013) 828–837.